Incorporation of SiC on the mechanical properties, tribological performance, and oxidation resistance of HfC-SiC/a-C:H coatings prepared by hybrid HiPIMS and pulsed-DC magnetron co-sputtering

Huan Luo[1], Hui Sun[2,*], Xiaolei Ye[3,*], Peipei Wang[1], Xing Zhao[1], Pascal Briois[4], Alain Billard[4]

[1] School of Materials Science and Engineering, Xi'an University of Science and Technology, Xi'an 710054, China

[2] Shandong Key Laboratory of Optical Astronomy and Solar-Terrestrial Environment, School of Space Science and Physics, Shandong University, Weihai, Shandong, 264209, China

[3] Faculty of Metallurgical and Energy Engineering, Kunming University of Science and Technology, Kunming, 650093, China

[4] FEMTO-ST Institute (UMR CNRS 6174), UBFC/UTBM, Site de Montbéliard, F-90010 Belfort, France

[*]Corresponding authors: Hui Sun; Xiaolei Ye

Abstract:

The multiphase nanocomposite HfC-SiC/a-C:H coatings consisting of HfC and SiC grains dispersed in the amorphous carbon matrix were deposited by hybrid HiPIMS and pulsed-DC magnetron co-sputtering. The incorporation of SiC ranging from 0 to 21.3 at.% on the chemical bonding state, nanocomposite structure, mechanical and tribological properties, and oxidation resistance of the coatings were explored. Results showed that the increase of SiC content is mainly at the expense of a-C:H matrix rather than nanocrystalline HfC, and is accompanied by changes in the HfC crystallinity. Nanohardness of up to 45 GPa was obtained for the HfC-SiC/a-C:H coating with 6.6 at.% SiC content. The optimum wear rate of $6.4 \times 10^{-7}\ \mathrm{mm}^3/\mathrm{N}$ and friction coefficient of 0.2 were also obtained at 6.6 at.% SiC content. The oxidation resistance is enhanced with the increase of SiC content, which delays the oxidation temperature by 100 °C with respect to the HfC/a-C:H coating.

Keywords: HiPIMS; HfC-SiC/a-C:H coating; Mechanical properties; Oxidation resistance.

1. Introduction

Transition metal carbon-based nanocomposite coatings (MeC/a-C:H) are known for their composite structures in which carbide grains are embedded in an amorphous carbon matrix, which endows the coating with many excellent properties, such as high hardness, excellent wear resistance, and good thermal shock resistance [1-3]. These attractive properties make MeC/a-C:H coating an ideal candidate for protective coating in the fields of cutting tools, engine contact friction components, and mold manufacturing, and has been widely used. Moreover, the hardening and wear mechanisms involved in their practical applications, such as those of TiC/a-C:H [4,5], WC/a-C:H [6,7], etc., have been intensively investigated by the academic community. Among many carbon-based nanocomposite coatings, HfC/a-C:H coating has the advantages of high hardness, high modulus, and strong thermal stability, due to the high melting point (3890°C), high strength and thermal shock resistance of the carbide grain Hafnium carbide (HfC) in the composite structure, making it one of the best protective coating materials [8,9]. In our previous work, HfC/a-C:H coating has been demonstrated to exhibit excellent mechanical properties and tribological performance [10]. However, its insufficient oxidation resistance is one of the current challenges, which severely limits its service life as a protective coating, especially under contact engineering and high-temperature conditions [11,12]. Thus, it is crucial to break through the insufficient oxidation resistance of the HfC/a-C:H coatings. Moreover, further improving the mechanical properties and tribological performance of the HfC/a-C:H coating to adapt to the rapid development of current high-end precision manufacturing is also urgently required. Therefore, the development of a novel carbon-based nanocomposite HfC/a-C:H coating that integrates improved higher mechanical properties, stronger wear protection, and sufficient oxidation resistance is pressing needed.

Of varied methods of improving the coating properties, the new phase addition is one of the most straightforward strategies [13,14]. On the one hand, rational selection of the new phase can tailor the favourable structure for desired properties, thus accessing the improved performance we need due to the properties of coating depending largely on the microstructure. On the other hand, the intrinsic properties of the new phase can be selectively exploited to compensate for some performance deficiencies of the original coating that to be improved. Silicon carbide (SiC), with excellent chemical inertness, high hardness, high thermal stability as well as strong oxidation resistance [15,16], is a good choice for the new phase to be incorporated into the transition metal carbide system, especially in modulating the mechanical properties and antioxidant capacity. S. Ghadami et al. [17] studied the mechanical properties of the SiC-reinforced HfB_2-based composite prepared by pressureless sintering. The results confirmed that the hardness and fracture toughness were enhanced at the 20 vol% SiC due to the increased relative density. Jose L. Endrino et al. [18] conducted an investigation of the microstructure and phase evolution of WC-SiC coatings with different SiC content and showed that the appropriate SiC content was beneficial to densifying the coating structure and improving the hardness.

Inspired by the advantages of SiC phase addition, the combination of HfC/a-C:H and SiC, namely, the HfC-SiC/a-C:H, should be a promising multiphase nanocomposite structure with stronger mechanical properties and excellent oxidation resistance. However, to our current knowledge, the multiphase nanocomposite HfC-SiC/a-C:H coatings have not been explored and reported so far. High power impulse magnetron sputtering (HiPIMS) is an advanced coating preparation technology, which is famous for its unique high-voltage impulsed discharge mode and high energy density characteristic of the sputtering plasma. Thanks to these features, HiPIMS can provide flexible and multi-dimensional control means for atomic-scale manipulation and fine-tuning of nanostructures for some specific property requirements during coating growth. Moreover, HiPIMS technology has outstanding advantages in the preparation of nanocomposite coatings for protective functional applications, including high density, high uniformity, and high strength [19]. Therefore, HiPIMS is expected to have remarkable potential in the preparation of multiphase nanocomposite HfC-SiC/a-C:H coatings.

In the present work, a series of multiphase nanocomposite HfC-SiC/a-C:H coatings with varying SiC content are deposited by the hybrid HiPIMS and pulsed-DC magnetron co-sputtering. To obtain this structure, an attempt to incorporate Si as a SiC phase-forming element into HfC/a-C:H is conducted. The mechanical and tribological properties, as well as oxidation resistance of HfC-SiC/a-C:H coatings with controlled SiC content are investigated. Parallel with the studies of these properties, the microstructural evolution is discussed in detail for a better understanding of the hardening, wear, and antioxidant mechanisms as an effort to search for a rational nanocomposite structure design for optimized performances.

2. Experimental details

2.1. Coating deposition

The HfC-SiC/a-C:H coatings with varying SiC content were fabricated using the hybrid sputtering system combining HiPIMS and Pulsed-DC magnetron sputtering. The Hf target and Si target with the same dimension of 150 mm in diameter and 6 mm in thickness, powered by HiPIMS and pulsed-DC in unipolar mode, were sputtered under the reactive mode of Ar and acetylene (C_2H_2) atmosphere. The C_2H_2 was used as the carbon source gas and its flow rate was kept constant at 18 standard cubic centimetres per minute (sccm). Substrates, including M2 disc, silicon wafer and stainless steel slide, were placed on a $\varnothing$=300 mm substrate stage and positioned 10 cm away from the sputtering target surface. The substrate stage is bias-free throughout the coating deposition process.

To improve the adhesion of the coating to the substrate, the Ar ion bombardment cleaning with a substrate bias of -700 V for 10 minutes and the pure Hf buffer layer deposition with 150 nm thick were pre-done. During the deposition of the Hf buffer layer, the cathode discharge voltage of -600 V during pulse time-on and the average discharge current of 2 A were used. The pulse duration (ton) was 47 μs while the pulse frequency was 500 Hz. The deposition time of the Hf buffer layer was controlled at 15 mins. The Ar gas at the flow rate of 200 sccm was introduced to provide the pressure of 0.4 Pa. Throughout the deposition process, including the pure Hf buffer layer and HfC-SiC/a-C:H coating, the rotating substrate stage was fixed at the speed of 30 revolutions per minute (r.p.m). During the HfC-SiC/a-C:H coating deposition, the discharge voltage of -600 V during 52 μs pulse time-on and the average discharge current of 2 A for the Hf target were used. The discharge current of the Si target ranging from 0 to 0.5 A with 0.1 A step increment was used to modulate the SiC concentration in the HfC-SiC/a-C:H coatings. The total thickness of the coating increases gradually with the raising Si target current (i.e., raising SiC content), distributed between 1.7 μm and 2.3 μm.

2.2. Coating characterization

Thermo Scientific Theta Probe X-ray Photoelectron Spectroscopy (XPS) was employed to analyze the elemental composition and chemical bonding state of the HfC-SiC/a-C:H coatings. The charge calibration was performed by setting the binding energy of the C 1s photoelectron peak to 285 eV. On the premise of not affecting the sample composition, the samples were cleaned by Ar ion bombardment to preferentially remove the contamination layer on the coating surface before measurement. The crystalline structure of the coatings was examined by a BRUKER D8 X-ray diffractometer (XRD) operated at a scanning speed (2θ) of 0.1 $^{\circ}s^{-1}$. Depending on the diffraction spectrum, the grain size was calculated through Scherrer's equation. Field Emission Scanning Electron Microscope (FESEM) (Jeol JSM-7800F) operated at 5 kV voltage was used to observe the fracture cross-sectional morphology and 15 kV voltage with energy dispersive X-ray spectroscopy (EDS) was used to measure the coating composition and elemental mapping.

The residual stress of HfC-SiC/a-C:H coatings with different SiC content was calculated by the Stoney equation, and its detailed testing and calculation process can be found in our previous work [20]. The nanohardness and Young's modulus of HfC-SiC/a-C:H coatings were studied using a Nanoindentation Tester (CSM Instruments) with a Berkovitch-type pyramidal diamond tip in continuous stiffness measurements mode. Twelve indentations were made for each sample to determine average hardness and modulus values. The indentation depth was controlled within one-tenth of the coating thickness to avoid substrate influence. Tribological tests were performed by using a CSM tribometer with a ball-on disk configuration at room temperature and relative humidity of 39 ± 3%. WC balls with a diameter of 6 mm were used as counter-bodies. A contact track radius of 3 mm, a sliding speed of 10 cm/s, a normal load of 2 N and a sliding laps of 10000 laps were established as testing parameters. The oxidation resistance of coatings was performed under air atmosphere at different temperatures, from 200 °C up to 700 °C with an incremental step of 100 °C, in the furnace of Nabertherm with a dwell time of 2 h. After annealing, X-ray diffraction, SEM, and EDS were used to determine the development of oxidation products and oxidation degree of the HfC-SiC/a-C:H coatings.

3. Results and discussion

3.1 Chemical bonding state

To gain insight into the atomic bonding evolution, the HfC-SiC/a-C:H coatings with varying SiC content are characterized by XPS. The elemental chemical states and chemical compositions are given in Fig. 1 and Table 1, respectively. When the discharge current of the Si target increases from 0 to 0.5 A, the SiC content in the HfC-SiC/a-C:H coating rises from 0 to 21.3 at% (from Table 1). In the present work, the HfC-SiC/a-C:H coatings are named by the SiC content they contain.

From Fig. 1(a), the narrow scan of Hf 4f spectra shows two spin-orbit doublets located at 14.2 eV (Hf $4f_{7/2}$) and 15.9 eV (Hf $4f_{5/2}$), corresponding to the C-Hf bonds [21]. Meanwhile, other Hf-related bonds were not detected and the C-Hf peaks were not shifted with increasing SiC content. It means that as SiC is incorporated into HfC-SiC/a-C:H coating, Si is not bonded to Hf. This indicates that there is no solid solution of Si into HfC or the formation of Hf-Si. In the C 1s spectra (Fig. 1(b)), the peaks centred at binding energy of 281.2 eV, 282.5 eV, 283.2 eV, 284.5 eV, and 285.4 eV are present, accounting for the Hf-C, Hf-C*, S i-C,sp^2-C and sp^3-C bonds, respectively [22-24]. Traces amounts of oxidized carbon present at 286.9 eV, corresponding to the C-O bond. In the Si 2p spectra (Fig. 1(c)), only one peak located at 100.5 eV is identified, which is assigned to the Si-C bond [25], implying that Si atoms are only bonded to C atoms but not to Hf atoms. Therefore, combining the above spectra of Hf 4f, Si 2p and C 1s results, it is demonstrated that the added Si atoms do not occupy the C sublattice vacancies in the non-stoichiometric HfC grains to form the solid solution of Hf(C, Si), but prefer to bond with hybrid carbon atoms of the a-C:H matrix to form a hybrid structure of HfC and SiC. The introduction of Si atoms thus leads to the formation of the multiphase nanocomposite structured coating consisting of crystalline HfC and SiC, a-C:H matrix, and a small number of oxides, namely HfC-SiC/a-C:H coating. Unlike the Si-added TaC coatings reported by Zhang et al. [26] in which Si atoms occupy C vacancies to form Ta(C, Si) solid solutions, Si atoms are not solid-dissolved into the HfC lattice in the present work.

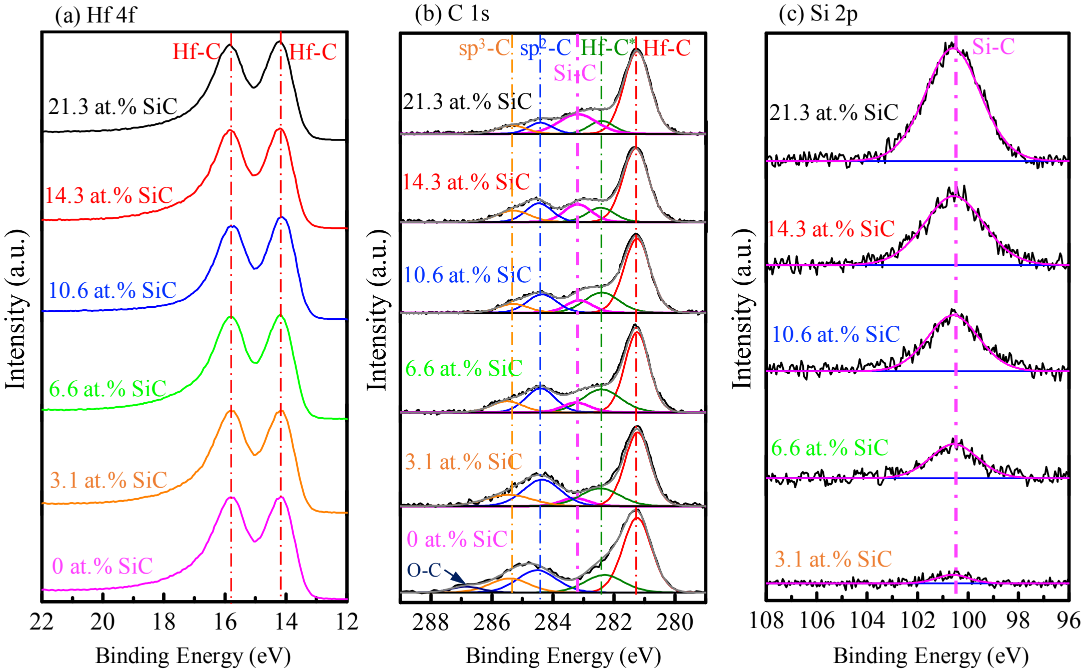

Figure 1. High-resolution XPS spectra of (a) Hf 4f (b) C 1s (c) Si 2p for the HfC-SiC/a-C:H coatings.

Based on the quantitative evolution trend of each peak in C 1s spectra and chemical composition, the fraction of each phase in HfC-SiC/a-C:H coating is calculated and shown in Table 1. The stoichiometric ratio x of the HfC$_x$ grain is calculated by excluding the amount of C binding to elements other than Hf. In Table 1, it can be observed that as the Si target current grows, the a-C:H content presents a decreasing trend from 21.2 to 6.9 at.% while the SiC content shows a rising trend. At the same time, the crystalline HfC content appears a slight increase from 60.5 to 62.5 at.% with the rise of SiC content. The decrease of a-C:H content is due to the fact that the introduction of Si is mainly at the expense of reducing the C content rather than the Hf content in the coating chemical composition. Moreover, Si atoms preferentially replace C atoms of the a-C:H matrix phase. Therefore, based on sacrificing the a-C:H matrix, the contents of HfC and SiC are increased. Further details point out that the decline rate of sp^2-C fraction (from 21.4 to 7.2 at.%) is faster than that of sp^3-C fraction (from 14 to 6.6 at.%) with increasing SiC content, suggesting that the Si atoms preferentially substitute the hybridized carbon atoms in sp^2-C rather than those in sp^3-C. Benefiting from this, the sp^3/sp^2 ratio in the a-C:H matrix is increased, which is beneficial to the hardness of the a-C:H matrix of the coating [27]. Similar phenomena have also been reported in the literature [28]. In addition, the C-Hf* content gradually decreases from 18.3 to 9.3 at.%, which is caused by the decrease of a-C:H content. Since the C-Hf* peak originates from the core electrons of the interface between a-C:H and crystalline HfC phases [29], the reduced a-C:H content leads to a smaller interface fraction between a-C:H and HfC phases, thus resulting in less core electron and lower C-Hf* content [30]. The stoichiometric ratio x of HfC$_x$ grain ranges from 0.95 at 0 at.% SiC to 0.57 at 21.3 at.% SiC. Besides, although there is no dispute that the SiC content is steadily increasing as the Si target current rises, in terms of the atomic arrangement of SiC (crystalline or amorphous), XRD needs to be combined for analysis.

Table 1. The relative amount of chemical bonds of C-Hf, C-Hf*, C-Si, sp^2-C and sp^3-C in C 1s spectra, and the total content of SiC, a-C:H, as well as stoichiometric ratio x of HfC$_x$ grains of the HfC-SiC/a-C:H coatings.

Si target current	Composition [at.%]			Types of bonding for C 1s [at.%]					HfC [at.%]	HfC* [at.%]	SiC [at.%]	a-C:H [at.%]	x in HfC$_x$
	Hf	C	Si	C-Hf	C-Hf*	C-Si	sp^2	sp^3					
0 A	40.3	59.7	0	48.2	14.6	0	21.4	14	60.5	18.3	0	21.2	0.95

0.1 A	39.7	57.4	2.9	49.3	14.6	2.6	20	13.5	59.9	17.7	3.1	19.3	0.88
0.2 A	38.9	55.5	5.6	50.8	14.4	5.6	17.3	11.9	60.1	17.0	6.6	16.3	0.84
0.3 A	38	54.2	7.8	53.4	12.5	9.3	14.2	10.6	61.5	14.4	10.6	13.5	0.79
0.4 A	37.5	52.4	10.1	54.4	10.2	12.6	13	9.8	62.0	11.6	14.3	12.1	0.69
0.5 A	36.6	49.1	14.3	57.8	8.6	19.8	7.2	6.6	62.5	9.3	21.3	6.9	0.57

3.2 Microstructure and Morphology

The microstructure of HfC-SiC/a-C:H coatings with SiC content varying from 0 to 21.3 at.% is investigated by XRD. According to the XRD diffraction spectrum, combined with the Scherrer formula, the grain size of HfC and SiC grains of the HfC-SiC/a-C:H coatings are calculated [31]. Both of them are shown in Fig. 2. For a more comprehensive analysis of the microstructure evolution of the coating, the content of the a-C:H matrix is also given in Fig. 2(b).

The coating with zero SiC content exhibits four distinct diffraction peaks at 38.9°, 45.3°, 65.9° and 79.3°, corresponding to (111), (200), (220) and (311) reflections of the fcc HfC phase (ICDD PDF#39-1491), respectively. With the increase of SiC content, the coating presents a distinguishable coexistence structure of the HfC phase and SiC phase. Among them, the SiC phase (ICDD PDF#29-1131) is dominated by the (101) orientation located at 39.9°. For the HfC-SiC/a-C:H coatings with SiC contents from 3.1 to 10.6 at.%, an increase in the intensity of the HfC peak accompanied by a narrowing of the full width at half maximum (FWHM) is observed. It corresponds to the coarsening of the HfC grains, from 6.4 nm at SiC-free content to the maximum size of 17.3nm at 10.6 at.% SiC content (Fig. 2(b)). Meanwhile, the SiC grains show a less obvious trend of refinement. Here, the HfC grain coarsening is attributed to the decreasing a-C:H matrix content (from 21.2 to 6.9 at.%, listed in Table 1) which weakens the inhibitory effect on the HfC grain growth embedded in it. This is consistent with the driving cause of the increased HfC content indicated by XPS results.

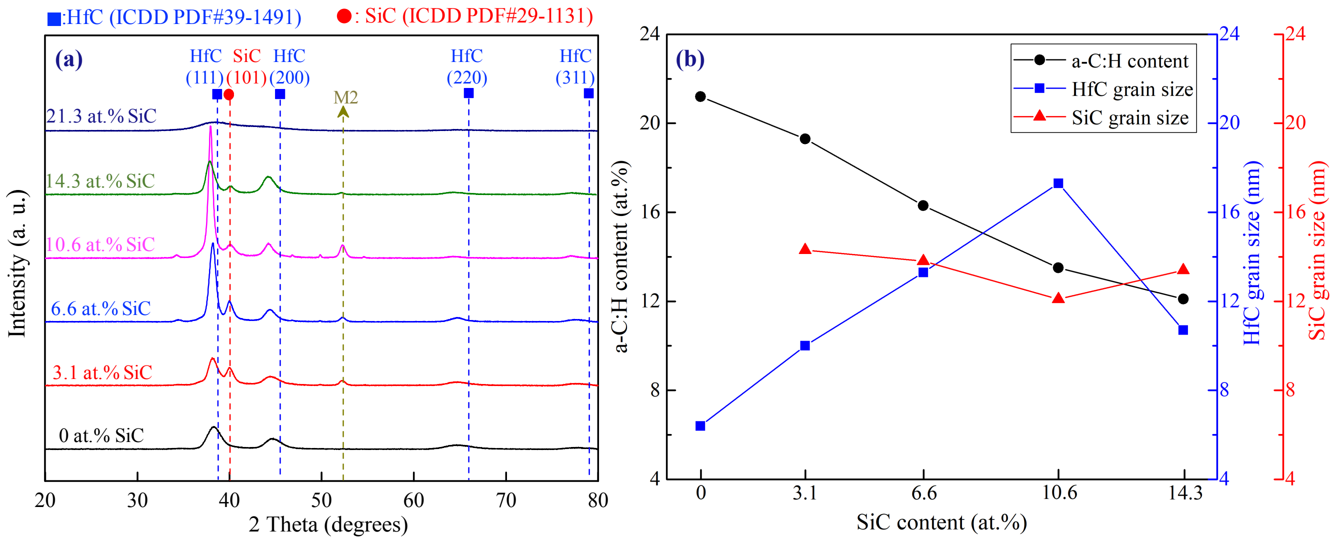

Figure 2. (a) X-ray diffractograms of HfC-SiC/a-C:H coatings with different SiC content, (b) grain size of HfC and SiC, as well as a-C:H matrix content as a function of SiC content.

As the SiC content increases to 14.3 at.%, the intensity of the HfC peak begins to weaken and thus the grain size decreases significantly, while the SiC grain size becomes larger, showing the evolution trends completely opposite to those of the coatings with low SiC content. Combined with the XPS results presented in Table 1, it is noticed that the increment of SiC content from 10.6 to 14.3 at.% is mainly compensated by the decrease of HfC^* content. At this time, the loss rate of a-C:H matrix content is slower, and the inhibiting effect of a-C:H matrix on the grain size of HfC thus becomes significant. Moreover, the SiC content above a certain threshold also interrupts the growth of HfC grains and forces newly arriving HfC-forming particles to renucleate [32]. Therefore, the HfC grains start to get smaller. Besides, due to the competition among the three phases of HfC, SiC and a-C:H matrix in the nanocomposite structure, the consequence of HfC grain refinement is that the relatively ample space is released for SiC growth, thus resulting in increased SiC grain size. At the highest SiC content of 21.3 at.%, the weak crystalline contribution of two phases HfC and SiC can be observed, both have an almost amorphous structure. On the one hand, it is associated with higher SiC content which could trigger the disordering effect [33], thus strongly changing the coating microstructure. On the other hand, under the high silicon target current conditions, the excessive processing on the growing coating by the plasma bombardment with high flux and high average energy may cause structure amorphization of the coating.

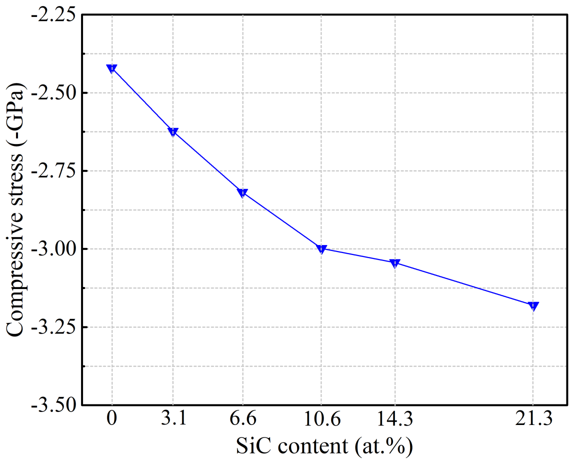

Figure 3. The compressive stress of HfC-SiC/a-C:H coatings as a function of SiC content.

In addition to the grain size evolution, the low angular shift of the HfC(111) peak with increasing SiC content is notable. For the non-equilibrium deposition condition of magnetron sputtering, the shift of the HfC(111) peak usually comes from three aspects, including the change of solid solubility of Si atoms in HfC grains, the change of carbon vacancies (reflected by the stoichiometric ratio of HfC_x), and the residual stress of coating. However, it is already known from XPS results that the Si atom is not solid-dissolved into the HfC lattice under our deposition conditions. Also, the C vacancies in the HfC lattice become more with increasing SiC content, evidenced by the decreased stoichiometric ratio x (indicated in Table 1). This will result in a high angular shift of the HfC(111) peak, contrary to the observed trend. Therefore, it is inferred that the shift of the HfC(111) peak comes only from the residual stress of the coating. To ensure that the observed shifting is supported by the residual stress induced by SiC addition, the residual stress of HfC-SiC/a-C:H coatings as a function of SiC content is measured, shown in Fig. 3. It can be seen that the residual stress of the coating is compressive, and gradually increases with the rising SiC content, confirming that the contribution of the low-angle shift of the HfC(111) peak is the buildup of residual compressive stress. This compressive stress with increasing SiC content may originate from the volume variation induced by the formation of crystalline phase SiC [34].

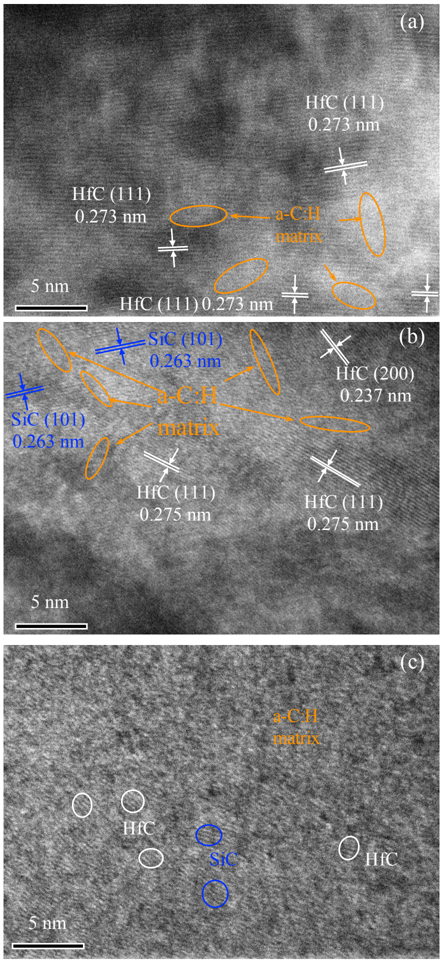

Figure 4. HRTEM images of HfC-SiC/a-C:H coatings with SiC content of (a) 0 at.%, (b) 6.6 at.%, and (c) 21.3 at.%.

Further TEM characterization of the HfC-SiC/a-C:H coatings is performed, shown in Fig. 4, for a more detailed evaluation of the microstructure. In Fig. 4(a), the a-C:H phase is marked by the orange oval area, while the crystalline HfC phase is indicated by the distinct diffraction fringes. It can be seen that the SiC-free coating exhibits a distinct nanocomposite structure consisting of HfC grains embedded in the a-C:H matrix, where the lattice spacing of 0.273 nm corresponds to the HfC(111) peak. When the 6.6 at.% SiC is introduced, the HfC-SiC/a-C:H coating (Fig. 4(b)) shows multiphase and polycrystalline characteristics, including HfC(111), HfC(200), SiC(101) grains and a-C:H matrix phase. Both HfC and SiC grains are separated by the a-C:H matrix. Among them, the lattice spacing of SiC(101) is 0.263 nm, marked by blue symbols, agreeing with the SiC peaks appearing in XRD. The lattice spacing corresponding to the HfC(111) peak increases to 0.275 nm, which is consistent with the low-angle shift of the HfC(111) peak indicated by

XRD. For the coating with 21.3 at.% SiC content (Fig. 4(c)), the structure presents a large amount of amorphous phase with very fine HfC and SiC grains, which corresponds to the quasi-amorphous structure shown by XRD, demonstrating the disordering effect of SiC on the nanocomposite structure of the coating [35].

Based on the above XPS, XRD and TEM characterizations and discussions, the evolution of the microstructure of HfC-SiC/a-C:H coatings with the change of SiC content is deduced. When Si is introduced into HfC/a-C:H coating, Si atoms preferentially bond with carbon atoms of sp^2-C in the a-C:H matrix and form a SiC phase, resulting in a multiphase nanocomposite structure consisting of HfC and SiC grains dispersed in the a-C:H matrix. As the SiC content increases, the multiphase nanocomposite structure of HfC-SiC/a-C:H coating is dominated by the competing results of SiC, HfC, and a-C:H matrix phases. When the SiC content is lower than 10.6 at.%, the a-C:H content decreases, while the HfC grains coarsen. When the SiC content exceeds 10.6 at.%, the SiC grain grows slightly and the HfC grain refines. As the SiC content continues to increase to 21.3 at.%, the coating structure begins to be disordered and exhibits an amorphous structure.

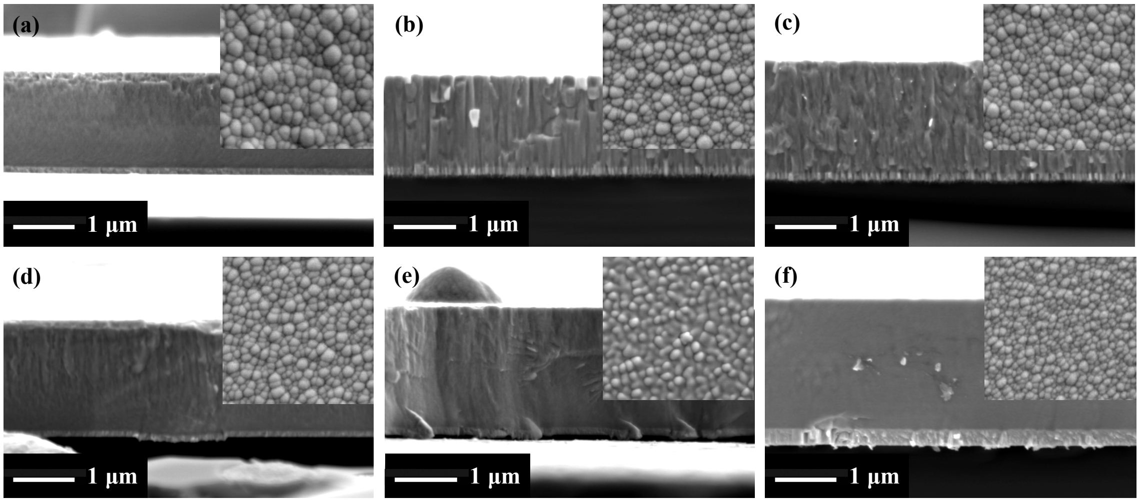

Figure 5. SEM micrographs of cross-sections and top-views for the HfC-SiC/a-C:H coatings with SiC content of (a) 0 at.%, (b) 3.1 at.%, (c) 6.6 at.%, (d) 10.6 at.%, (e) 14.3 at.%, and (f) 21.3 at.%.

Surface and cross-sectional morphologies of HfC-SiC/a-C:H coatings with varying SiC content are characterized and presented in Fig. 5. The coating morphology is strongly dependent on the SiC content. For the coating without SiC, the coating surface exhibits a dome-like morphology. However, with the appearance of SiC, the coating surface morphology evolves to a flatter topography with finer particles, indicating a monotonic decrease in roughness. At the high SiC content of 21.3 at.% (Fig. 5(f)), the coating surface becomes smoother with the distribution of smaller particles on it, which is supported by the smoothing effect of the amorphous structure of the coating. For the growth morphology of the coating brittle fracture cross-section, it turns from a typical long penetrated columnar structure at 3.1 at.% SiC to shorter columnar crystals at 6.6 at.% SiC, similar to the vertical continuous growth of columnar crystals being interrupted. Afterwards, as the SiC content increases to 21.3 at.%, the coating morphology gradually transitions to a featureless glassy character, consistent with the amorphous structure demonstrated by XRD and TEM.

3.3 Mechanical properties

Fig. 6 (a) shows the nanohardness and Young's modulus of the HfC-SiC/a-C:H coatings as a function of SiC content. The hardness of HfC/a-C:H alone is 33.2 GPa. For the coatings with a small addition of SiC content ranging from 0 to 6.6 at.%, the hardness increases significantly with increasing SiC content and reaches the maximum value of 45 GPa at 6.6 at.%. However, higher SiC content addition instead leads to poorer hardness. Even after the SiC content exceeds 14.3 at.%, the hardness of the coating becomes lower than that of SiC-free coating. Young's modulus of the HfC-SiC/a-C:H coating exhibits a similar evolution trend to the hardness.

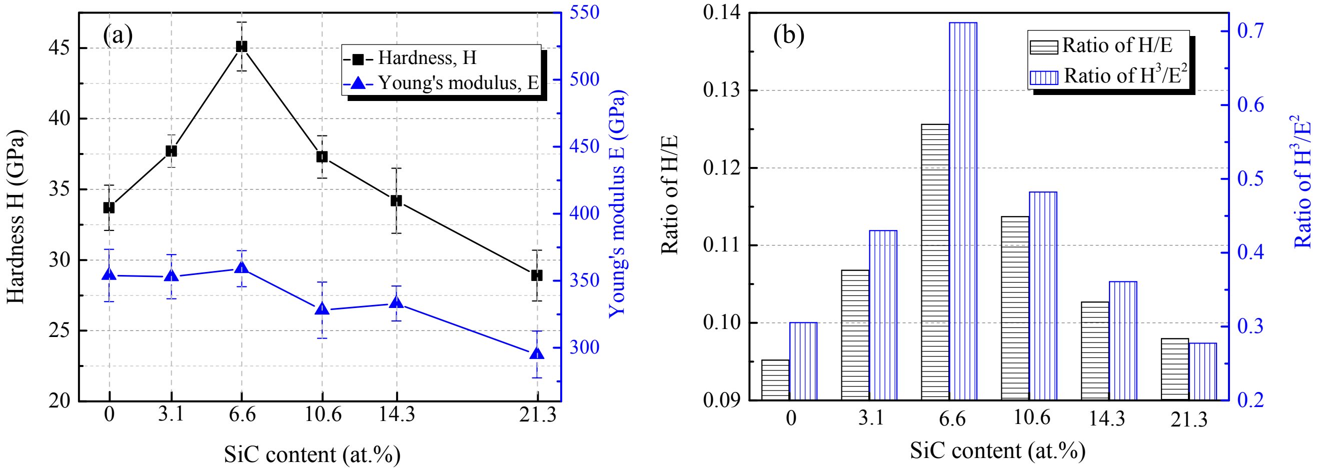

Figure 6. The hardness H, Young's modulus E and ratios H/E and H^3/E^2 of the HfC-SiC/a-C:H coatings with various SiC content.

As the SiC content increases from 0 to 6.6 at.%, the HfC grain size increases from 6.4 nm to 13.4 nm, located in the interval of the reverse Hall-Petch relation [36], where the larger the nanocrystal size, the higher the hardness. Meanwhile, the newly formed SiC content gradually increases and its grain size is maintained at around 14 nm. The content of the a-C:H matrix decreases. Under the comprehensive effect of the above HfC, SiC and a-C:H three phases evolutions, the nanocomposite structure consisting of both crystalline HfC and SiC grains uniformly embedded in the a-C:H matrix changes accordingly. That is, the mean grain separation provided by the a-C:H matrix gradually narrows, while the grain sizes of the HfC and SiC tend to be close. It is known that the appropriate mean grain separation and a small amount of uniformly distributed SiC phase could act as the hindrance to grain displacement or deformation [29][37], thus leading to the increase of hardness in the range of 0 to 6.6 at.% SiC content. Moreover, the formation of the SiC phase leads to a decrease in the sp^2/sp^3-C ratio of the a-C:H matrix (from XPS results), thus increasing the hardness of the a-C:H matrix. This is also conducive to the hardness enhancement of the HfC-SiC/a-C:H coating, although the amplitude of the enhancement is small. Therefore, for the maximum hardness at 6.6 at.% SiC content, its main contribution is inferred to be derived from the unique multiphase nanocomposite structure characteristic: homogeneously dispersed HfC and SiC grains (with suitable size ~14 nm) in the a-C:H matrix with enhanced autogenous hardness. In addition, the coating hardness also depends on the residual stress state of the coating. It has been demonstrated in Fig. 3 that the increase of SiC content leads to the accumulation of residual compressive stress in the HfC-SiC/a-C:H coating. This compressive stress accumulation would promote an increase in the energy of the coating on the microscopic scale, thus contributing to hardness enhancement.

When the SiC content increases to 10.6 at.%, the mean grain separation of the nanocomposite structure tends to be excessively narrow, which is synergistically caused by the continuous increase in HfC and SiC content, as well as the decreasing a-C: H content. Under this condition, both the suppression of grain displacement and the grain incoherent strain, induced by the proper mean grain separation filled with a-C:H matrix, would be weakened. Consequently, the unique nanocomposite structure that could provide high hardness is broken, thus the decreased hardness is observed. As the SiC content continues to increase to 21.3 at.%, the coating transitions from the multiphase nanocomposite structure to the amorphous structure. The high hardness provided by the crystalline phases HfC and SiC with the a-C:H matrix disappears, pushing the hardness of the coating down.

According to the evolution trends of hardness H and Young's modulus E, the ratios of H/E and H^3/E^2 as a function of SiC content are displayed in Fig. 6 (b). The maximum values of H/E and H^3/E^2 also appear at 6.6 at.% SiC content, which are 0.119 and 0.64, respectively. It indicates that the coating containing 6.6 at.% SiC processes the best toughness and resistance against plastic deformation among all the samples we prepared [38]. Therefore, it is reasonable to expect that this coating will perform optimally in tribological properties [39].

3.4 Tribological performance

The dynamic friction curves of HfC-SiC/a-C:H coatings with varying SiC content as a function of sliding laps are presented in Fig. 7. The coefficient of friction (COF) values are taken from the average of the friction curves, marked with the blue symbol and placed adjacent to each of dynamic friction curve.

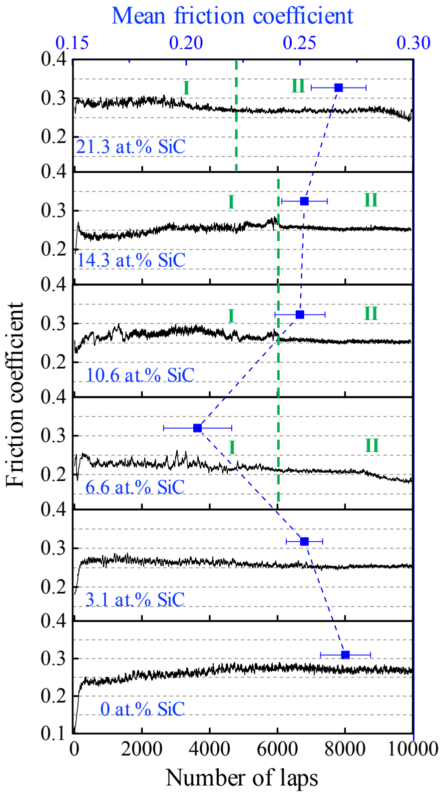

Figure 7. The dynamic friction curves (black one) of HfC-SiC/a-C:H coatings with different SiC content as a function of the sliding cycle and the COF values (blue one).

For the coating without SiC content, the dynamic friction curve shows a steady evolution trend with an increasing number of sliding cycles. The amplitude of the fluctuations (i.e., burrs) appearing on it is uniform, no matter in the running-in phase or stable plateau phase of the friction test process. As the SiC content is introduced and increased to 3.3 at.%, the fluctuation amplitude on the friction curve becomes smaller, indicating a smoother and more stable contact friction process. With the further increase in SiC content, the friction curves of all coatings with SiC content exceeding 6.6 at.% present two different stages, which are distinguished as Region I and Region II, marked by the green-dotted lines in Fig 7. Region I of the friction curve (before 6000 sliding cycles) is accompanied by relatively obvious fluctuations, which is attributed to the decrease of sp^2-C content with increasing SiC content. Since the sp^2-C of the a-C: H matrix promotes the faster formation of the easily sheared tribo-layer, the less the amount of sp^2-C, the more intense the run-in fluctuation. Moreover, the presence of Si in the coating would suppress the degree of graphitization of the a-C:H matrix (sp^3-C conversion to sp^2-C) during the initial friction process [28], resulting in rough spikes appearing on the friction curves. Therefore, the run-in-like fluctuations in Region I are more pronounced. Regarding Region II of the friction curve, the fluctuations on it are significantly reduced, even smoother than that of SiC-free coating. It may be due to the fact that tribochemical reactions are activated once the sliding cycle reaches a certain level. At the moment, the silicon-containing tribo-layer would be formed, which could compensate for the weakened self-lubrication effect caused by the reduced sp^2-C [40]. To elucidate the tribochemical reaction and the presence of silicon-containing tribo-layer, the chemical nature of the wear track of the HfC-SiC/a-C:H coatings with 0 and 21.3 at.% SiC is characterized by XPS respectively, shown in Fig. 8. In the O 1s core energy spectra (Fig. 8(a)), the peaks centred at 529.8 eV, 533.0 eV and 534.5 eV are observed on the spectrum of the HfC-SiC/a-C:H coating with 0 at.% SiC, which can be identified as O-Hf, C=O and C-O-C phase [41][42]. Compared with the coating without SiC content, three new peaks located at 531.5 eV, 531.9 eV and 532.8 eV appear in the spectra of the HfC-SiC/a-C:H coating with 21.3 at.% SiC. Wang H et al. [43] and Kumar A et al. [44] have pointed out that the formation of the peak at 531.5 eV was attributed to the presence of the hafnium silicate phase. Based on this, the peak of 531.5 eV is inferred to correspond to the formation of the hafnium silicate phase Hf-Si-O. Moreover, the other two peaks located at 531.9 eV and 532.8 eV are assigned to the Si-O and SiO_2 phases. Therefore, it can be confirmed that after a certain sliding cycle test, the tribochemical reaction is activated and the silicon-containing tribo-layer is formed. For the Si 2p core energy spectra (Fig. 8(b)), the Si-C, O-Hf-Si, Si-O and SiO_2 phases form on the wear track of the HfC-SiC/a-C:H coating with 21.3 at.% SiC, evidenced by the peaks located at 100.5 eV, 101.9 eV, 102.9 eV and 103.8 eV [45], respectively. It further corroborates the formation of silicon-containing tribo-layer. Therefore, it can be determined that the smoother and more stable COF dynamic curve is contributed by the silicon-containing tribo-layer formed on the wear track.

From the baseline of the stable plateau period of the dynamic friction curve, it can be seen that the coefficient of friction (COF) of the coating first decreases and then increases in the interval [0.2, 0.27] with the increasing SiC content. The minimum COF value of 0.2 is achieved at 6.6 at.% SiC content. It is known that for carbon-based nanocomposite coatings, the sp^2-C content in the a-C:H matrix is one of the key factors dominating the COF. The higher the sp^2-C content, the lower the COF. However, in the present work, as the SiC content increases, the sp^2-C content decreases continuously, while the COF presents a trend of first decreasing and then increasing. Therefore, it can be determined that sp^2-C is not the dominant factor for the HfC-SiC/a-C:H coating. Based on Fig. 6, it can be found that the mechanical properties of HfC-SiC/a-C:H coatings determine its evolution trend as a function of SiC content in perfect agreement with that of the COF value. Therefore, it can be stated that the COF of the HfC-SiC/a-C:H coating is dominated by the mechanical properties rather than the contribution from the amorphous carbon matrix property (sp^2-C content).

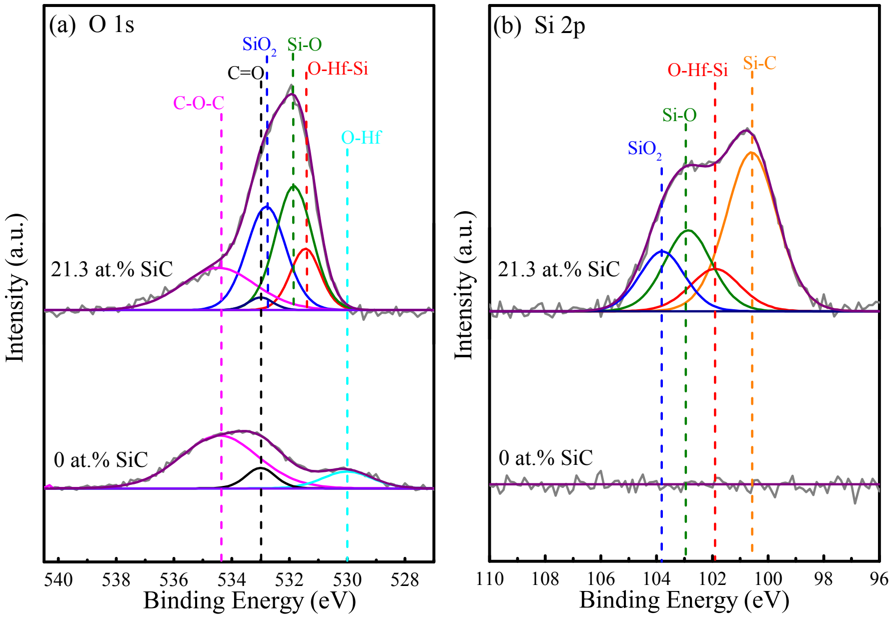

Figure 8. XPS core level spectra of (a) O 1s and (b) Si2p performed on the wear tracks for HfC-SiC/a-C:H coatings with 0 at.% SiC content and 21.3 at.% SiC content.

The wear rates of all the HfC-SiC/a-C:H coatings are calculated and summarized in Fig. 9(a). Meanwhile, the corresponding morphology and profile of each wear track are given in Fig. 9(b)-(g). The wear rate and the COF show a consistent evolution trend. As the SiC content increases from 0 to 6.6 at.%, the wear rate decreases from 6.96×10^{-6} to $6.38 \times 10^{-7}\ \mathrm{mm}^3/\mathrm{N}$. The corresponding wear tracks become shallower and narrower significantly, where the severe grooves on the wear track gradually transition to smoother one and the profile with the conspicuous sawtooth-like spikes distribution (displayed in the upper right corner position) transforms into a more rounded concave distributed profile. The enhanced wear rate in this interval is due to the improvement of the mechanical properties indicated by H, H/E, and H^3/E^2 (discussed in section 3.3), which afford smaller sliding contact surface between the counterpart ball and the coating surface, less indentation depth under applied load and greater resistance against abrasion by wear debris, as well as the stronger ability to dissipate energy during plastic deformation, thereby resulting in less wear loss [46].

When the SiC content continues to increase from 10.6 to 21.3 at.%, the wear rate presents a reverse upward trend from 1.67×10^{-6} to $2.02 \times 10^{-6}\ \mathrm{mm}^3/\mathrm{N}$. The corresponding wear tracks are gradually widened, accompanied by the deepening of the grooves on it (Fig. 9(e)-(g)). It is attributed to the decreased hardness and toughness (characterized by H/E) from 10.6 to 21.3 at.% SiC, making these coatings more susceptible to abrasion. In addition, it is noteworthy that although there is a dramatic decline rate in the mechanical properties of the coating with SiC content from 10.6 to 21.3 at.%, and the hardness at 21.3 at.% is even lower than that of the coating without SiC content (indicated by the slope of the hardness evolution in Fig. 6), the wear rate deteriorates only slightly. This slightly worsened wear rate may be contributed by the formation of a Si-containing tribo-layer, as indicated in Fig. 8, which is beneficial to reduce the sliding shear resistance and thus reduce the degree of wear to a certain extent. The weakening effect of poor mechanical properties on the wear rate is thus properly compensated. Therefore, it can be deduced that the wear rate of HfC-SiC/a-C:H coating is dominated by the synergy of mechanical properties and tribochemical reactions.

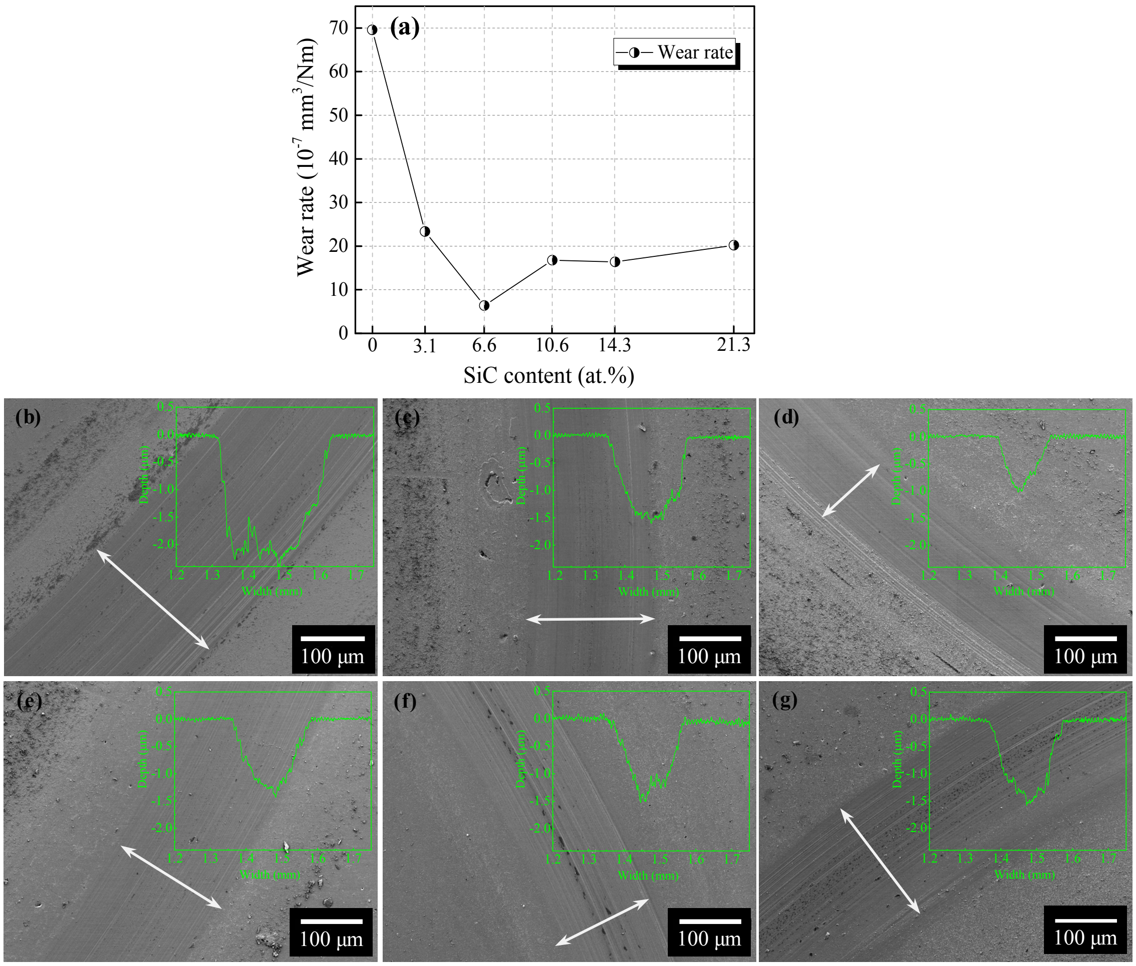

Figure 9. (a) Wear rates and corresponding morphologies and profiles of wear tracks for the HfC-SiC/a-C:H coatings with (b) 0 at.%, (c) 3.1 at.%, (d) 6.6 at.%, (e) 10.6 at.%, (f) 14.3 at.%, and (g) 21.3 at.% SiC content.

The optimum wear resistance is possessed by the coating with 6.6 at.% SiC, which is derived from the best mechanical properties held by this coating and the proper SiC content [47]. The corresponding morphology and profile of the wear track confirm that the narrowest and shallowest wear track is distributed on the coating with 6.6 at.% SiC. Besides, it is noticed that the grooves can be observed on the wear tracks of all HfC-SiC/a-C:H coatings. It is because the hardness of all coatings is at a relatively high level (harder than 30 GPa), the wear debris shed during the friction process is thus difficult to deform and could scratch the coating surface as the destructive grinding body under the continual periodic sliding.

3.5 Oxidation resistance

The HfC-SiC/a-C:H coating was tested at 600 and 700°C in an air environment for 2h to evaluate the coating oxidation resistance. After the oxidation test, the phase structure, morphology and composition of the oxidation products of the HfC-SiC/a-C:H coatings were characterized to judge the oxidation degree. Note that the sample used in the oxidation test was the coating deposited on the M2 substrate, which is thicker than the coating deposited on the Si wafer shown in Fig. 5.

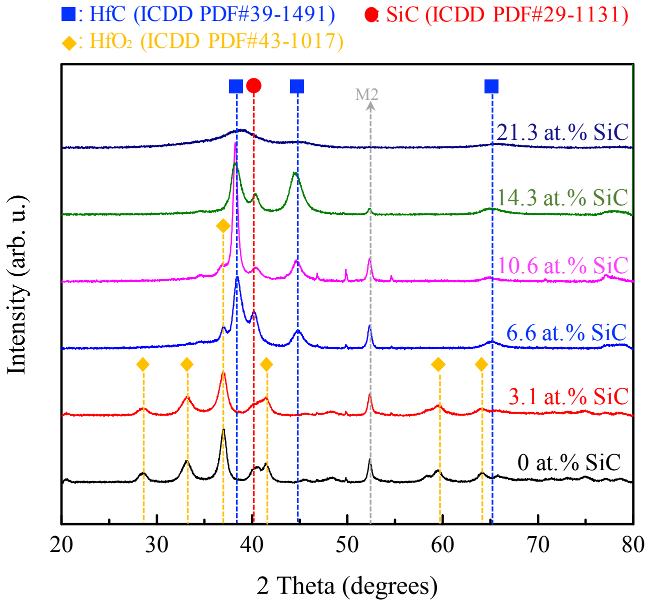

Figure 10. X-ray diffractograms of HfC-SiC/a-C:H coatings with different SiC content after 600 °C oxidation resistance test.

Fig. 10 presents the phase evolution of the HfC-SiC/a-C:H coated M2 substrate after oxidation at 600°C for different SiC content. There is no HfC peak observed in the two coatings with 0 and 3.1 at.% SiC, clearly resolvable diffraction peaks are assigned to the HfO_2 phase (marked by yellow diamonds) and the SiC phase (marked by red circles). For the other two coatings that have 6.6 and 10.6 at.% SiC, the main diffraction peaks HfC and SiC coexist with a small amount of HfO_2 diffraction peak. Upon further increasing the SiC content, the diffraction spectra of the coatings with 14.3 and 21.3 at.% SiC are almost the same as those of as-deposited HfC-SiC/a-C:H coatings, containing only HfC and SiC peaks. No oxide-related diffraction peaks are detected. However, it should be noted here that the absence of oxidation peaks may be due to the limitations of XRD detection techniques. No oxide peak does not mean that the coating remains intact and has not been oxidized at all. Nevertheless, one can preliminarily infer that the degree of oxidation reaction is relatively weak in these two coatings. In addition, for the $HfO_2(111)$ peak located at 36.9°, its FWHM becomes larger and its intensity decreases as the SiC content increases, corresponding to the finer oxide grains and reduced oxide crystallinity [48]. This finer grain is supported by the presence of the unoxidized SiC phase which has an inhibitory effect on the growth of oxide phase. Meanwhile, this change in crystallinity and grain size may be accompanied by changes in the growth morphology and density characteristic of the oxide scale on the coating surface. Further analysis will be performed by morphology characterization of SEM.

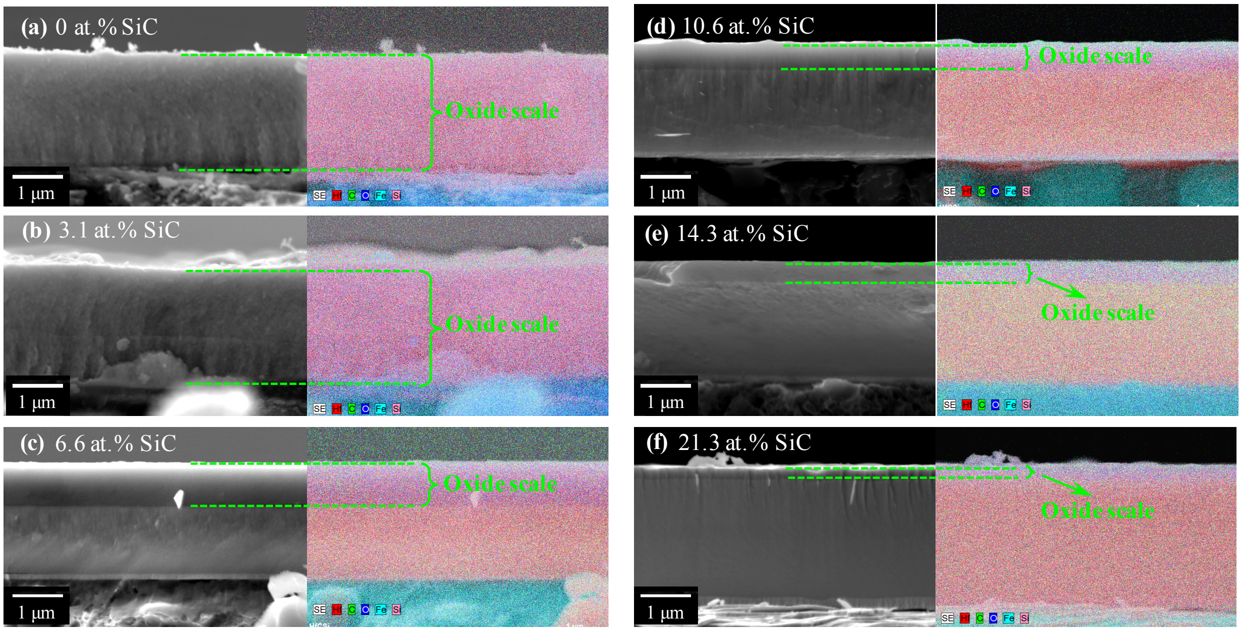

Figure 11. The cross-sectional SEM images and corresponding EDS maps of HfC-SiC/a-C:H coatings with varying SiC content after 600 °C oxidation resistance test.

To further clarify the oxidation degree of the HfC-SiC/a-C:H coating, the cross-sectional morphology and elemental mapping as a function of SiC content of the oxidized samples are analyzed, displayed in Fig. 11. After oxidation at 600 °C for 2 h, the coating adhesion remains good and no cracking or spalling of the coating is observed. Consistent with the XRD results, the first two coatings with 0 and 3.1 at.% SiC content are completely oxidized. The oxide scale thickness of the other coatings with SiC content $\geqslant$ 6.6 at.% decreases monotonically with SiC content, from about ~1 µm to 210 nm. Different from XRD results, the coatings with 14.3 and 21.3 at.% SiC have a clearly thin oxide scale, which means that oxidation of all coatings is activated. Besides, it can be seen that the morphology of the oxide scale becomes denser gradually with the rise of SiC content, transitioning from a loose granular structure to a dense glassy feature. Such a denser structure is more effective in blocking oxygen diffusion into the coating interior. Therefore, it is confirmed that increasing the SiC content leads to an enhanced oxidation resistance of the HfC-SiC/a-C:H coating. It is consistent with the information indicated by the phase evolution trend displayed in XRD diffraction spectra.

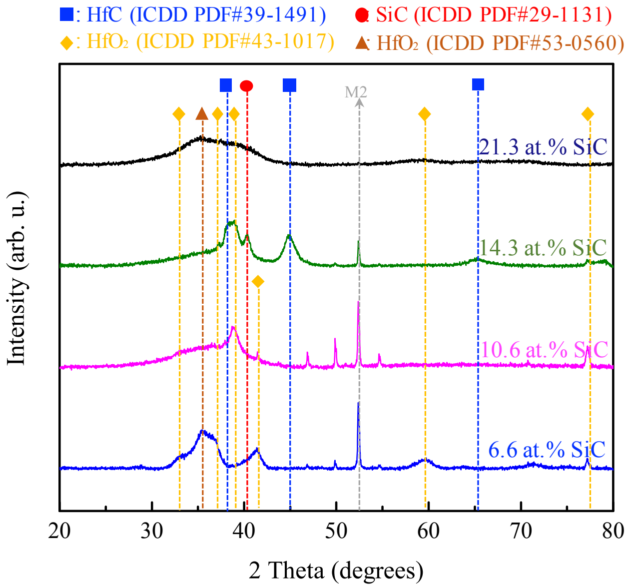

Figure 12. X-ray diffractograms of HfC-SiC/a-C:H coatings with different SiC content after 700 °C oxidation resistance test.

When the HfC-SiC/a-C:H coating was oxidized at 700 °C in an air atmosphere, the coatings with 0 and 3.1 at.% SiC content were completely oxidized and the oxidation products have been exfoliated, exposing the M2 substrate that also suffered from oxidation. Based on this point, the characterization results of these two coatings are not presented, the characterizations of the remaining four coatings with higher SiC content are exhibited in Figs. 12 and 13, respectively. After oxidation at 700 °C, the HfC peak of the coating containing 6.6 at.% SiC can not be detected, accompanied by the distinguishable HfO_2 peaks, confirming the occurrence of more severe oxidation. As the SiC content further increases, the intensity of the HfO_2 peak is compressed, and the HfC and SiC peaks gradually become resolvable (marked by the blue rectangle and the red circle), which proves that SiC enhances the oxidation resistance of HfC-SiC/a-C:H coating. In addition, it is worth noting that the SiC peak is always observable, even in fully oxidized coatings (such as the coating with 0 and 3.1 at.% SiC after 600 °C oxidation in Fig.10 and the coating with 6.6 at.% SiC after 700 °C oxidation in Fig. 11). This is provided by the chemical inertness and strong oxidation resistance of the SiC phase.

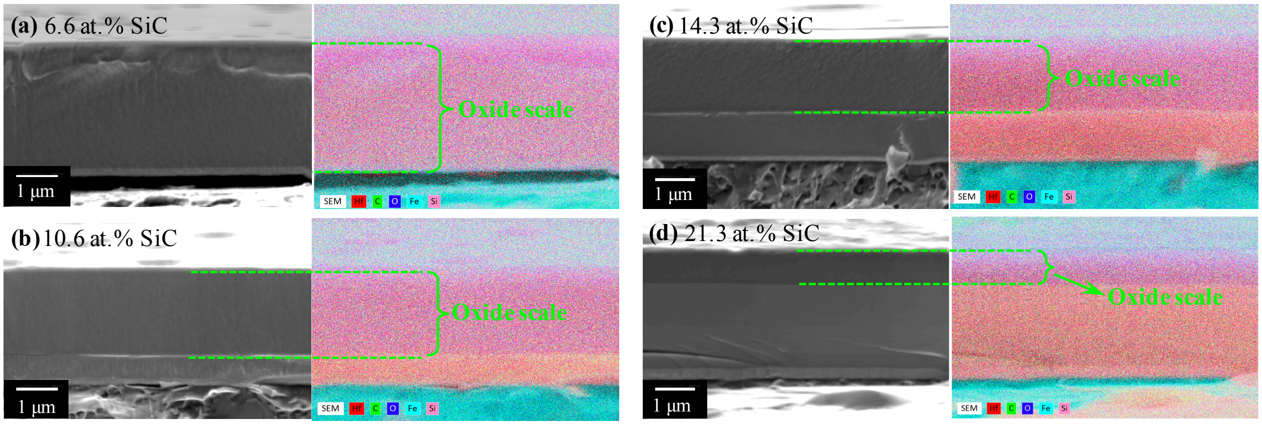

Figure 13. The cross-sectional SEM images and corresponding EDS maps of HfC-SiC/a-C:H coatings with varying SiC content after oxidation resistance at 700 °C.

The cross-sectional SEM images and corresponding EDS maps of HfC-SiC/a-C:H coating after 700 °C oxidation are depicted in Fig. 13. It is obvious that the oxidation degree of the coating is exacerbated at 700 °C, as evidenced by the thicker oxide scale under the same SiC content compared with the coating after 600 °C oxidation, indicating that the oxidation degree of HfC-SiC/a-C:H coating is increased with the increase of oxidation temperature. It results from a faster oxygen diffusion rate at higher temperatures. The thickness and the growth morphology of the oxide scale show the same evolution trends as those of the oxide scale formed after the 600 °C oxidation test. The higher the SiC content, the thinner the oxide scale thickness and the denser the growth morphology, thus acting as a more effective barrier to oxygen diffusion. According to them, it is concluded that the oxidation of HfC-SiC/a-C:H coating is controlled by the in-ward oxygen diffusion through the HfO_2 layer formed on top of the coating. The presence and increase of the SiC phase allow the formation of a denser barrier layer, thus exhibiting a reinforcement effect on the antioxidation of HfC-SiC/a-C:H coating.

Our previous work on nanocomposite HfC/a-C:H coatings already confirmed that the higher the proportion of a-C:H matrix, the worse the oxidation resistance of HfC/a-C:H coating [10]. Its oxidation process starts from the erosion of the a-C:H matrix, gradually reaches the HfC grains, and finally oxidizes and consumes the HfC grains. Based on this, an anticipated strategy to enhance the oxidation resistance is to partially replace the a-C:H matrix with a new chemically inert and oxidation-resistant phase. Therefore, adding the SiC phase to form the multiphase nanocomposite HfC-SiC/a-C:H coating consisting of HfC and SiC grains uniformly dispersed in a-C:H matrix is proposed and implemented in the present work. The enhanced oxidation resistance is attributed to the incorporation of the SiC phase into the composite structure, which affords a double beneficial effect. On the one hand, the SiC incorporation reduces the fraction of a-C:H matrix (especially the sp^2-C inside), which is easy to oxidize and escape [49], without damaging (enhancing inversely) the mechanical properties and tribological performance of the coating. This could effectively reduce the rapid oxidation loss of amorphous carbon at the initial oxidation stage and the size of the subsequent oxygen diffusion channels left behind [50]. On the other hand, the SiC phase dispersed between HfC grains plays its intrinsic role as a diffusion barrier, which could retard oxygen atoms migration and oxygen erosion into the HfC grains, thereby enhancing the oxidation resistance of the coating [51]. In addition, since the uniform dispersion of unoxidized SiC grains could hinder the coarsening of HfO_2 grains during the oxidation process [52], the dense growth of the oxide scale is promoted, which is also a key factor in improving the oxidation resistance. In summary, the incorporation of the SiC phase and the formation of the multiphase nanocomposite structure are the fundamental reasons for the improvement of the oxidation resistance of HfC-SiC/a-C:H coating, which substantially prevents oxygen diffusion from three aspects: the reduction of easily oxidizable sp^2-C fraction, the intrinsic diffusion barrier characteristic of SiC grains, and the increase of the density of oxide scale.

4. Conclusion

To further improve the mechanical and tribological properties of the carbon-based nanocomposite HfC/a-C:H coating and to overcome its application defect of insufficient oxidation resistance synergistically, the design strategy for incorporation of SiC to form a multiphase nanocomposite structure HfC-SiC/a-C:H was proposed and implemented through the hybrid HiPIMS and pulsed-DC magnetron co-sputtering. The incorporation of SiC content on the chemical bond state, phase composition, composite structure and growth morphology of the HfC-SiC/a-C:H coating was investigated systematically. Parallel with the studies of these coating structure characteristics, the mechanical and tribological properties, as well as oxidation resistance of HfC-SiC/a-C:H coatings were discussed in detail. It is found that the unique multiphase nanocomposite structure, in which hard HfC and SiC grains are homogeneously dispersed in the a-C:H matrix, is the reason giving rise to the overall highest hardness and toughness for the coating with 6.6 at.% SiC content. The results regarding the tribological performance reveal that the best friction coefficient and wear resistance of HfC-SiC/a-C:H coatings is achieved at 6.6 at.% SiC content, which is determined synergistically by the sp^2-C- and Si-related tribochemical reactions and mechanical properties. The oxidation resistance of the HfC-SiC/a-C:H coating is enhanced monotonously with the increase of SiC content, benefiting from the preferential substitution of sp^2-C, intrinsic diffusion barrier characteristic, and oxide scale densification effect caused by the incorporation of SiC. The oxidation temperature is delayed by 100 °C with respect to the HfC/a-C:H coating. The present work demonstrates that the SiC incorporation and its modulation on the multiphase nanocomposite structure is a promising and effective strategy for making high-performance coatings integrating superhard, low friction, wear resistance and oxidation resistance.

Declaration of Competing Interest

The authors declare that they have no competing financial interests or personal relationships that could have appeared to influence the work reported in this paper.

Acknowledgements

The authors thank the Natural Science Basic Research Plan in Shaanxi Province of China (2022JQ-551), the National Key R&D Program of China (2022YFB3706600, 2022YFE0123000), the National Natural Science Foundation of China (62004117), and the Natural Science Basic Research Plan in Shaanxi Province of China (Grant No. 2022JQ-354) for their financial support of this study.

References

[1] N. Sala, et al., Nb-C thin films prepared by DC-MS and HiPIMS: Synthesis, structure, and tribomechanical properties, Surf. Coat. Tech. 422 (2021) 127569, https://doi.org/10.1016/j.surfcoat.2021.127569

[2] H. Q. Wang, et al., Tribocorrosion behaviors of nc-TiC/aC: H nanocomposite coatings: In-situ electrochemical response, Thin Solid Films 730 (2021) 138719, https://doi.org/10.1016/j.tsf.2021.138719

[3] H. Sun, A. Billard, H. Luo, W. T. Zheng, X. L. Zheng, M. J. Dai, F. Sanchette, Influence of carbon content on the mechanical properties of TiCN-Cu nanocomposite coatings prepared by multi-arc ion plating, Vacuum 187 (2021) 110139, https://doi.org/10.1016/j.vacuum.2021.110139

[4] B. S. Lou, Y. T. Hsiao, L. C. Chang, W. Diyatmika, J. W. Lee, The influence of different power supply modes on the microstructure, mechanical, and corrosion properties of nc-TiC/aC: H nanocomposite coatings, Surf. Coat. Tech. 422 (2021) 127512, https://doi.org/10.1016/j.surfcoat.2021.127512

[5] H. Larhlimi, O. Abegunde, Y. Samih, A. Ghailane, M. Makha, J. Alami, Effect of carbon content on the structural, mechanical and corrosion properties of TiC films deposited using a HiPIMS discharge, Surf. Coat. Tech. 451 (2022) 129028, https://doi.org/10.1016/j.surfcoat.2022.129028

[6] S. Soltanahmadi, T. Charpentier, I. Nedelcu, V. Khetan, A. Morina, H. M. Freeman, A. Neville, Surface fatigue behavior of a WC/aC: H thin-film and the tribochemical impact of zinc dialkyldithiophosphate, ACS appl. materials & interfaces 11 (2019) 41676-41687, https://doi.org/10.1021/acsami.9b14669

[7] D. He, Y. Zhao, W. Li, L. Shang, L. Wang, G. Zhang, Superior mechanical and tribological properties governed by optimized modulation ratio in WC/aC nano-multilayers, Ceram. Int. 47 (2021) 16861-16869, https://doi.org/10.1016/j.ceramint.2021.02.261

[8] Z. Y. Tan, J. W. Guo, W. Zhu, Ablation resistance of HfC-TaC-$Hf_6Ta_2O_{17}$ composite coatings prepared by vacuum plasma spraying, Corros. Sci. (2023) 111368, https://doi.org/10.1016/j.corsci.2023.111368

[9] J. Xu, W. Sun, X. Xiong, H. Zhang, L. Yang, High-quality SiC-HfC coating with interpenetrating structure based on a two-step low temperature molten salt method, J. Eur. Ceram. Soc. 43 (2023) 5054-5060, https://doi.org/10.1016/j.jeurceramsoc.2023.04.001

[10] H. Luo, H. Sun, F. Gao, A. Billard, Mechanical properties, thermal stability and oxidation resistance of HfC/aC: H films deposited by HiPIMS, J. Alloy. Compd. 847 (2020) 156538, https://doi.org/10.1016/j.jallcom.2020.156538

[11] C. Poltorak, M. Stüber, H. Leiste, A. Bergmaier, S. Ulrich, Study of (Ti,Zr) C: H/aC: H nanocomposite thin film formation by low temperature reactive high power impulse magnetron sputtering, Surf. Coat. Tech. 398 (2020) 125958, https://doi.org/10.1016/j.surfcoat.2020.125958

[12] T. W. Hsu, G. Greczynski, R. Boyd, S. Kolozsvári, P. Polcik, M. Odén, Dense and hard TiWC protective coatings grown with tungsten ion irradiation using WC-HiPIMS/TiC-DCMS co-sputtering technique without external heating, Appl. Surf. Sci. 618 (2023) 156639, https://doi.org/10.1016/j.apsusc.2023.156639

[13] Z. Zhang, Q. Yang, Z. Yu, H. Wang, T. Zhang, Influence of Y_2O_3 addition on the microstructure of TiC reinforced Ti-based composite coating prepared by laser cladding, Mater. Charact. 189 (2022) 111962, https://doi.org/10.1016/j.matchar.2022.111962

[14] R. Zhao, C. Hu, Y. Wang, S. Pang, J. Li, S. Tang, H. M. Cheng, Construction of sandwich-structured C/C-SiC and C/C-SiC-ZrC composites with good mechanical and anti-ablation properties, J. Eur. Ceram. Soc. 42 (2022) 1219-1226, https://doi.org/10.1016/j.jeurceramsoc.2021.12.006

[15] L. Zhou, L. Zhu, T. Yang, X. Hou, Z. Du, S. Cao, Z. L. Wang, Ultra-stable and durable piezoelectric nanogenerator with all-weather service capability based on N doped 4H-SiC nanohole arrays, Nano-micro lett. 14 (2022) 1-10, https://doi.org/10.1007/s40820-021-00779-0

[16] H. Dong, Z. Fang, T. Yang, Y. Yu, D. Wang, K. C. Chou, X. Hou, Single crystalline 3C-SiC whiskers used for electrochemical detection of nitrite under neutral condition, Ionics 22 (2016) 1493-1500, https://doi.org/10.1007/s11581-016-1666-5

[17] S. Ghadami, E. Taheri-Nassaj, H. R. Baharvandi, F. Ghadami, Improvement of mechanical properties of HfB_2-based composites by incorporating in situ SiC reinforcement through pressureless sintering, Sci. Rep. 11 (2021) 9835, https://doi.org/10.1038/s41598-021-88566-0

[18] J. L. Endrino, J. E. Krzanowski, Nanostructure and mechanical properties of WC-SiC thin films, J. Mater. Res. 17 (2002) 3163-3167, https://doi.org/10.1557/JMR.2002.0457

[19] H. Larhlimi, A. Ghailane, M. Makha, J. Alami, Magnetron sputtered titanium carbide-based coatings: A review of science and technology, Vacuum 197 (2022) 110853, https://doi.org/10.1016/j.vacuum.2021.110853

[20] H. Luo, F. Gao, A. Billard, Effect of auxiliary magnetic field on the conformal coverage of the microtrenches in high power impulse magnetron sputtering, J. Mater. Process. Tech. 283 (2020) 116732, https://doi.org/10.1016/j.jmatprotec.2020.116732

[21] J. Cheng, X. Wang, H. Wang, C. Shao, J. Wang, Preparation and high-temperature behavior of HfC-SiC nanocomposites derived from a non-oxygen single-source-precursor, J. Am. Ceram. Soc. 100 (2017) 5044-5055, https://doi.org/10.1111/jace.15063

[22] M. Ahmed, M. Khawaja, M. Notarianni, B. Wang, D. Goding, B. Gupta, F. Iacopi, A thin film approach for SiC-derived graphene as an on-chip electrode for supercapacitors, Nanotechnology 26 (2015) 434005, https://orcid.org/0000-0002-3196-0990

[23] M. Rybachuk, J. M. Bell, Electronic states of trans-polyacetylene, poly (p-phenylene vinylene) and sp-hybridised carbon species in amorphous hydrogenated carbon probed by resonant Raman scattering, Carbon 47 (2009) 2481-2490, https://doi.org/10.1016/j.carbon.2009.04.049

[24] K. M. Jiang, D. Q. Zhao, X. Jiang, Q. Huang, L. J. Miao, H. M. Lu, Y. Li, Electronic-structure, corrosion and mechanical properties of nc-CrC/aC: H films deposited by multi-arc ion plating, J. Alloy. Compd. 750 (2018) 560-569, https://doi.org/10.1016/j.jallcom.2018.04.017

[25] G. Qin, R. Zhang, B. Makarenko, A. Kumar, W. Rabalais, J. M. L. Romero, C. Cai, Highly stable, protein resistant thin films on SiC-modified silicon substrates, Chem. Commun. 46 (2010) 3289-3291, https://doi.org/10.1039/B925708J

[26] S. Du, M. Wen, L. Yang, P. Ren, Q. Meng, K. Zhang, W. Zheng, Structural, hardness and toughness evolution in Si-incorporated TaC films, Ceram. Int. 44 (2018) 9318-9325, https://doi.org/10.1016/j.ceramint.2018.02.144

[27] A. W. Zia, M. Birkett, Deposition of diamond-like carbon coatings: Conventional to non-conventional approaches for emerging markets, Ceram. Int. 47 (2021) 28075-28085, https://doi.org/10.1016/j.ceramint.2021.07.005

[28] C. Q. Guo, S. S. Lin, D. Gao, Q. Shi, C. B. Wei, M. J. Dai, X. G. Zhu, Modulation of Si on microstructure and tribo-mechanical properties of hydrogen-free DLC films prepared by magnetron sputtering, Appl. Surf. Sci. 509 (2020) 145381, https://doi.org/10.1016/j.apsusc.2020.145381

[29] W. Shuo, Z. Kan, A. Tao, H. Chaoquan, M. Qingnan, M. Yuanzhi, W. Mao, Z. Weitao, Structure, mechanical and tribological properties of HfC_x films deposited by reactive magnetron sputtering, Appl. Surf. Sci. 327 (2015) 68-76, https://doi.org/10.1016/j.apsusc.2014.11.130.

[30] Q. N. Meng, M. Wen, F. Mao, N. Nedfors, U. Jansson, W. T. Zheng, Deposition and characterization of reactive magnetron sputtered zirconium carbide films, Surf. Coat. Technol. 232 (2013) 876-883, https://doi.org/10.1016/j.surfcoat.2013.06.116

[31] A. L. Patterson, The Scherrer formula for X-ray particle size determination, Physical review 56 (1939) 978, https://doi.org/10.1103/PhysRev.56.978

[32] N. Nedfors, O. Tengstrand, E. Lewin, A. Furlan, P. Eklund, L. Hultman, U. Jansson, Structural, mechanical and electrical-contact properties of nanocrystalline-NbC/amorphous-C coatings deposited by magnetron sputtering, Surf. Coat. Technol. 206 (2011) 354-359, https://doi.org/10.1016/j.surfcoat.2011.07.021

[33] T. Zehnder, J. Matthey, P. Schwaller, A. Klein, P. A. Steinmann, J. Patscheider, Wear protective coatings consisting of TiC-SiC-aC: H deposited by magnetron sputtering, Surf. Coat. Technol. 163 (2003) 238-244, https://doi.org/10.1016/S0257-8972(02)00477-2

[34] W. Hao, N. Ni, Y. Guo, C. Li, X. Fan, W. Xiao, P. Xiao, Densification, strengthening and toughening in hafnium carbide with the addition of silicon carbonitride, J. Am. Ceram. Soc. 103 (2020) 3286-3298, https://doi.org/10.1111/jace.16985

[35] K. Zhang, M. Wen, S. Wang, R.P. Deng, D. Gall, W.T. Zheng, Sputter deposited NbC_xNy films: effect of nitrogen content on structure and mechanical and tribological properties, Surf. Coat. Technol. 258 (2014) 746-753, https://doi.org/10.1016/j.surfcoat.2014.07.086

[36] S. N. Naik, S. M. Walley, The Hall-Petch and inverse Hall-Petch relations and the hardness of nanocrystalline metals, J. Mater. Sci. 55 (2020) 2661-2681, https://doi.org/10.1007/s10853-019-04160-w

[37] C. A. Charitidis, Nanomechanical and nanotribological properties of carbon-based thin films: A review, Int. J. Refract. Met. H. 28 (2010) 51-70, https://doi.org/10.1016/j.ijrmhm.2009.08.003

[38] X. Chen, Y. Du, Y. W. Chung, Commentary on using H/E and H^3/E^2 as proxies for fracture toughness of hard coatings, Thin Solid Films 688 (2019) 137265, https://doi.org/10.1016/j.tsf.2019.04.040

[39] B. D. Beake, The influence of the H/E ratio on wear resistance of coating systems-Insights from small-scale testing, Surf. Coat. Technol. 442 (2022) 128272, https://doi.org/10.1016/j.surfcoat.2022.128272

[40] I. W. Park, S. R. Choi, J. H. Suh, C. G. Park, K. H. Kim, Deposition and mechanical evaluation of superhard Ti-Al-Si-N nanocomposite films by a hybrid coating system, Thin Solid Films 447 (2004) 443-448, https://doi.org/10.1016/S0040-6090(03)01122-2

[41] A. Liu, Z. Guo, G. Liu, C. Zhu, H. Zhu, B. Shin, F. Shan, Redox chloride elimination reaction: facile solution route for indium-free, low-voltage, and high-performance transistors, Adv. Electron. Mater. 3 (2017) 1600513, https://doi.org/10.1002/aelm.201600513

[42] B. Sivaranjini, R. Mangaiyarkarasi, V. Ganesh, S. Umadevi, Vertical alignment of liquid crystals over a functionalized flexible substrate, Sci. Rep. 8 (2018) 8891, https://doi.org/10.1038/s41598-018-27039-3

[43] H. Wang, P. Wu, X. F. Li, S. Chen, S. P. Zhang, B. B. Song, Study of reactions between HfO_2 and Si in thin films with precise identification of chemical states by XPS, Appl. Surf. Sci. 257 (2011) 3440-3445, https://doi.org/10.1016/j.apsusc.2010.11.042

[44] P. Kaur, S. Kumar, C. L. Chen, et al., Investigations on structural, magnetic and electronic structure of Gd-doped ZnO nanostructures synthesized using sol-gel technique, Appl. Phys. A 122 (2016) 1-8, https://doi.org/10.1007/s00339-016-9707-5

[45] S. Ntais, V. Dracopoulos, A. Siokou, TiCl4(THF)2 impregnation on a flat SiO_x/Si(100) and on polycrystalline Au foil: Determination of surface species using XPS, J. Mol. Catal. A: Chem. 220 (2004) 199-205, https://doi.org/10.1016/j.molcata.2004.05.002

[46] J. Musil, Hard nanocomposite coatings: Thermal stability, oxidation resistance and toughness, Surf. Coat. Technol. 207 (2012) 50-65, https://doi.org/10.1016/j.surfcoat.2012.05.073

[47] F. Lomello, M. A. P. Yazdi, F. Sanchette, F. Schuster, M. Tabarant, A. Billard, Temperature dependence of the residual stresses and mechanical properties in TiN/CrN nanolayered coatings processed by cathodic arc deposition, Surf. Coat. Technol. 238 (2014) 216-222, https://doi.org/10.1016/j.surfcoat.2013.10.079

[48] K. He, N. Chen, C. Wang, L. Wei, J. Chen, Method for determining crystal grain size by x-ray diffraction, Cryst. Res. Technol. 53 (2018) 1700157, https://doi.org/10.1002/crat.201700157

[49] S. Osswald, G. Yushin, V. Mochalin, S. O. Kucheyev, Y. Gogotsi, Control of sp^2/sp^3 carbon ratio and surface chemistry of nanodiamond powders by selective oxidation in air, J. Am. Ceram. Soc. 128 (2006) 11635-11642, https://doi.org/10.1021/ja063303n

[50] S. Zhang, X. L. Bui, X. Li, Thermal stability and oxidation properties of magnetron sputtered diamond-like carbon and its nanocomposite coatings, Diam. Relat. Mater. 15 (2006) 972-976, https://doi.org/10.1016/j.diamond.2005.12.005

[51] G. Zeng, P. Xu, C. Zeng, C. Fang, Y. Wang, X. Yang, Q. Huang, Synthesis and pyrolysis of single-source precursor for HfC_xN_{1-x}-SiC ceramic with different SiC contents, Ceram. Int. 48 (2022) 22967-22974, https://doi.org/10.1016/j.ceramint.2022.04.263

[52] L. Hultman, Thermal stability of nitride thin films, Vacuum 57 (2000) 1-30, https://doi.org/10.1016/S0042-207X(00)00143-3